

Wigner-molecule supercrystal in transition metal dichalcogenide moiré superlattices: Lessons from the bottom-up approach

Constantine Yannouleas^{*} and Uzi Landman[†]

School of Physics, Georgia Institute of Technology, Atlanta, Georgia 30332-0430, USA



(Received 4 December 2023; accepted 29 February 2024; published 18 March 2024)

The few-body problem for $N = 4$ fermionic charge carriers in a double-well moiré quantum dot (MQD), representing the first step in a bottom-up strategy to investigate formation of molecular supercrystals in transition metal dichalcogenide (TMD) moiré superlattices with integral fillings, $\nu > 1$, is solved exactly by employing large-scale exact-diagonalization via full configuration interaction (FCI) computations. A comparative analysis with the mean-field solutions of the often used spin-and-space unrestricted Hartree-Fock (sS-UHF) method demonstrates the limitations of the UHF method (by itself) to provide a proper description of the influence of the interdot Coulomb interaction. In particular, it is explicitly shown for $\nu = 2$ that the exact charge densities (CDs) within each MQD retain the ringlike shape characteristic (for a wide range of relevant parameters) of a fully isolated MQD, as was found for *sliding* Wigner molecules (WMs). This deeply quantum-mechanical behavior contrasts sharply with the UHF CDs that portray solely orientationally pinned and well-localized dumbbell dimers. An improved CD, which agrees with the FCI-calculated one, derived from the restoration of the sS-UHF broken parity symmetries is further introduced, suggesting a beyond-mean-field methodological roadmap for correcting the sS-UHF results. It is conjectured that the conclusions for the $\nu = 2$ moiré TMD superlattice case extend to all cases with integral fillings that are associated with sliding WMs in isolated MQDs. The case of $\nu = 3$, associated with a pinned WM in isolated MQDs, is an exception.

DOI: [10.1103/PhysRevB.109.L121302](https://doi.org/10.1103/PhysRevB.109.L121302)

Introduction. Understanding the electronic spectral and configurational organization beyond that of natural atoms is rapidly becoming a major research direction focusing on the exploration of the nature of a few charged carriers trapped in artificially fabricated, isolated or superlattice-assembled, quantum dots (QDs) [1–3]. Such research is motivated by the potential for utilizing these systems, with high tunability and control, in future quantum information and computational platforms [4–7]. Earlier studies have unveiled a novel fundamental-physics aspect in such nanosystems, namely, formation of quantum Wigner molecules (WMs), originally predicted theoretically [8–33] in two-dimensional (2D) semiconductor QDs, as well as trapped ultracold atoms, and subsequently observed experimentally in GaAs QDs [34–37], Si/SiGe QDs [38], and carbon nanotubes [39]. Remarkably, recent work [40] extended the WM portfolio to the newly arising and highly pursued field of TMD moiré materials, owing mainly to the promise for fundamental-physics discoveries and the potential for advancing quantum-device applications.

Adopting a bottom-up methodology, and building on the demonstrated emergence [40] of WMs in the quasi-isolated moiré pockets [most often referred to as moiré quantum dots (MQDs)], we address here the inevitable incorporation of such single MQDs in a superlattice structure. Specifically, this Letter focuses on the effects on WM formation resulting from the interaction between neighboring MQDs. Two

different methodologies are used in this endeavor, namely: (i) the spin-and-space unrestricted Hartree-Fock (sS-UHF) [8,12,21,41,42] and (ii) the full configuration interaction (FCI) [15,16,21,24,28,29,33,43–47]. In particular, through a detailed comparison with the FCI *exact* results (serving here as comparative benchmarks), we show that except when the classical equilibrium configuration of the \tilde{n} confined carriers in each single MQD is commensurate with the trilobal symmetry of the moiré confinement (see below, leading to a pinned WM configuration, e.g., when $\tilde{n} = 3$), the sS-UHF approximation (by itself) is unreliable for investigations of WM-exhibiting moiré double quantum dots (MDQDs) in *unstrained* TMD bilayers (that is, in naturally occurring, bias-free cases). This deficiency dictates further corrective measures (beyond the mean-field sS-UHF) that are provided by the theory of restoration of broken symmetries and extensions thereof [12,19–21,41,44,48–50]. Specifically, for $\nu = 2$ and for a set of materials parameters suitable to moiré TMD superlattices, we show that, in spite of the interaction with a neighboring MDQ, the ground-state FCI charge densities within each MQD remain ringlike with a superimposed trilobal distortion, as in the case of a single isolated MQD [40] illustrated in the inset of Fig. 1(a). This contrasts sharply with the corresponding (mean-field) sS-UHF CD *prior* to symmetry restoration, which exhibits a pair of two antipodal and well-localized charge carriers.

On the other hand, the *symmetry-restored* UHF (SR-UHF) charge densities are in agreement with the exact (FCI) ones. These results suggest a much desired gateway for systematic large-scale computational studies of WM-MQD assemblies in

^{*}constantine.yannouleas@physics.gatech.edu

[†]Uzi.Landman@physics.gatech.edu

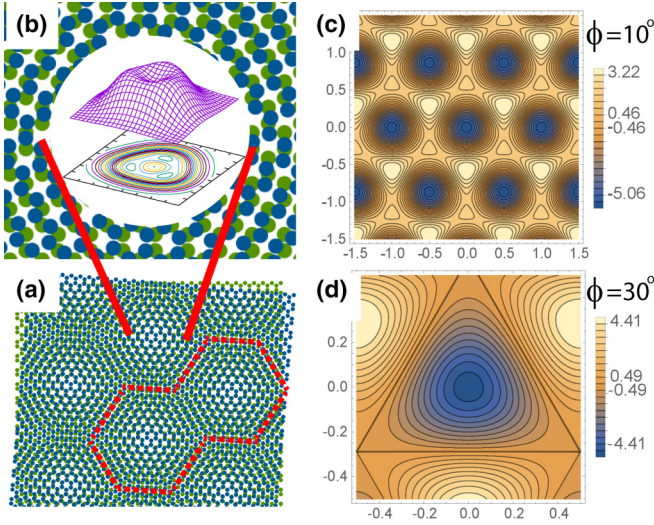


FIG. 1. (a) Schematic moiré pattern produced by two twisted monolayers. The area demarcated by the dashed red line corresponds to the isolated moiré *double* quantum dot investigated in this Letter. (b) The spin-singlet ground-state FCI charge density associated with $N = 2$ holes in a *single* isolated moiré quantum dot, exhibiting a ring-like shape with a trilobal distortion. This ringlike CD is characteristic of a *sliding* (contrasted to a *pinned*) Wigner molecule. Parameters used: effective mass $m^* = 0.9m_e$, dielectric constant $\kappa = 5$, strength of moiré modulation $v_0 = 10.3$ meV, moiré lattice constant $a_M = 9.8$ nm, trilobal distortion $\phi = 20^\circ$; see Eq. (1). These parameters are also used in all CD calculations (either FCI or UHF) for the MDQD case below. (c) Broader view of the moiré periodic potential structure given by Eq. (1) for an angle of $\phi = 10^\circ$. (d) Potential of a single moiré QD for $\phi = 30^\circ$. In panels (c) and (d), $v_0 = 15$ meV and $a_M = 14$ nm. Length units are in nanometers in panel (b) and in a_M in panels (c) and (d). The CD in panel (a) is in units of $1/\text{nm}^2$. All CDs in this Letter are normalized to $N = 4$.

TMD materials using a beyond-mean-field-corrected SR-sS-UHF methodology, capable of modeling systems comprised of a much larger number of carriers (electrons or holes) that may be treated with the exact-diagonalization, FCI, method. Furthermore, in light of rapid advances in STM imaging techniques [51,52], we expect that the FCI predictions shown here will gain verification in the near future (see *Note added* at the end).

Confinement potentials and many-body Hamiltonian. The potential confining the extra charge carriers at the pockets of the 2D moiré superlattice can be approximated by the expression [53–55]

$$V(\mathbf{r}) = -2v_0 \sum_{i=1}^3 \cos(\mathbf{G}_i \cdot \mathbf{r} + \phi), \quad (1)$$

where $\mathbf{G}_i = \{(4\pi/\sqrt{3}a_M)[\sin(2\pi i/3), \cos(2\pi i/3)]\}$ are the moiré reciprocal lattice vectors. The materials specific parameters of $V(\mathbf{r})$ are v_0 (which can also be experimentally controlled through voltage biasing), the moiré lattice constant a_M , and the angle ϕ . a_M is typically of the order of 10 nm, which is much larger than the lattice constant of the monolayer TMD material (typically a few Å). For the overall periodic-array structure of $V(\mathbf{r})$, see Fig. 1(c).

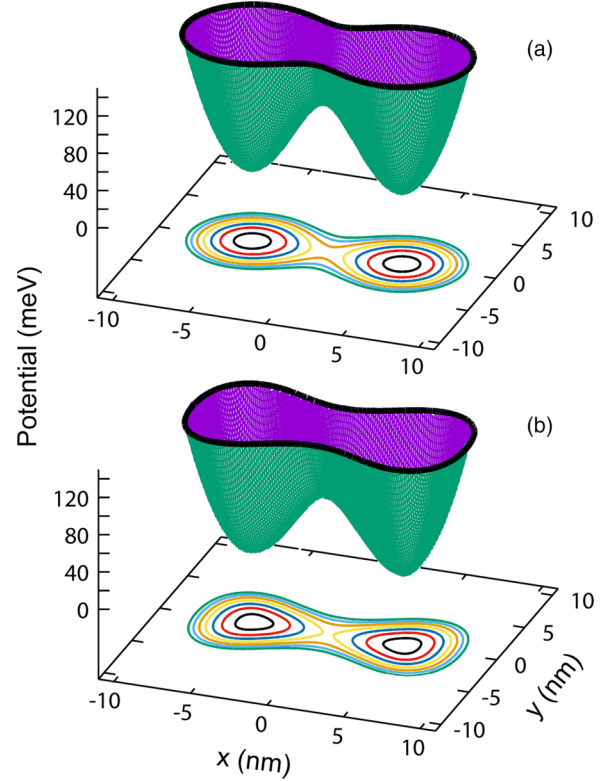


FIG. 2. The confining potential for the MDQD. (a) The TCO potential according to Eq. (3), which does not include the trilobal deformation. (b) The potential [Eq. (5)] for the MDQD, which does include the trilobal deformation within each QD. Parameters used: $\hbar\omega_0 = 36.71$ meV (which corresponds to $v_0 = 10.3$ meV, $a_M = 9.8$ nm, and $\phi = 20^\circ$), $-x_1 = x_2 = 4.9$ nm, $\epsilon^b = 0.44$, and $f = 0.15$. The interdot barrier is 84.07 meV in panel (a) and 71.46 meV in panel (b).

The parameter ϕ controls the strength of the trilobal C_3 crystal-field-type anisotropy in each MQD potential pocket [see Fig. 1(d)]. This anisotropy can be seen by expanding $V(\mathbf{r})$ in Eq. (1) in powers of r and defining an approximate confining potential, $V_{\text{MQD}}(\mathbf{r})$, for a single MQD as follows:

$$V_{\text{MQD}}(\mathbf{r}) \equiv V(\mathbf{r}) + 6v_0 \cos(\phi) \approx m^* \omega_0^2 r^2 / 2 + C \sin(3\theta) r^3, \quad (2)$$

where $m^* \omega_0^2 = 16\pi^2 v_0 \cos(\phi) / a_M^2$, $C = 16\pi^3 v_0 \sin(\phi) / (3\sqrt{3}a_M^3)$, m^* is the effective mass, and the expansion of $V(\mathbf{r})$ can be restricted to the terms up to r^3 . (r, θ) are the polar coordinates of the position vector \mathbf{r} .

We construct a potential confinement for an isolated *pair* of two neighboring MQDs [see the area marked by the thick dashed red border in Fig. 1(a)] in two steps.

First, we consider the potential of a two-center-oscillator (TCO) with a smooth neck [8,21,32,33,46,56], namely,

$$V_{\text{TCO}}(x, y) = \frac{1}{2} m^* \omega_y^2 y^2 + \frac{1}{2} m^* \omega_{xk}^2 x_k^2 + V_{\text{neck}}(x), \quad (3)$$

where $x'_k = x - x_k$ with $k = 1$ for $x < 0$ (left) and $k = 2$ for $x > 0$ (right). Here y denotes the coordinate perpendicular to the interdot axis (x). In this Letter, we take $\omega_{x1} = \omega_{x2} = \omega_y = \omega_0$, with ω_0 coinciding with that of a single MQD [see Eq. (2)].

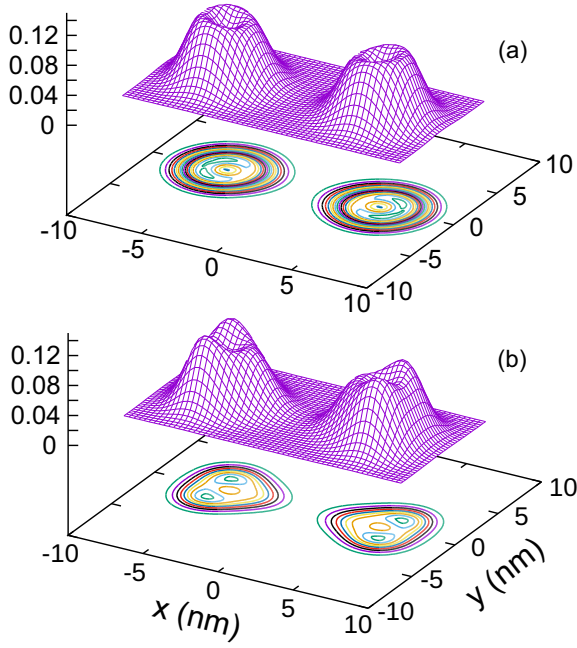


FIG. 3. Ground-state FCI charge densities for the case of the moiré double QD with $N = 4$ holes. (a) CD for the confinement in Fig. 2(a) (no trilobal deformation). (b) CD for the confinement in Fig. 2(b) (trilobal deformation included). Remaining parameters: effective mass $m^* = 0.90m_e$ and dielectric constant $\kappa = 5$. See text for a detailed description. CDs are in units of $1/\text{nm}^2$.

For the smooth neck, we use

$$V_{\text{neck}}(x) = \frac{1}{2}m^*\omega_0^2[C_k x_k'^3 + \mathcal{D}_k x_k'^4]\Theta(|x| - |x_k|), \quad (4)$$

where $\Theta(u) = 0$ for $u > 0$ and $\Theta(u) = 1$ for $u < 0$. The four constants C_k and \mathcal{D}_k can be expressed via two parameters, as follows: $C_k = (2 - 4\epsilon^b)/x_k$ and $\mathcal{D}_k = (1 - 3\epsilon^b)/x_k^2$, where the barrier-control parameter $\epsilon^b = V_b/V_0$ is related to the height of the targeted interdot barrier V_b , and $V_0 = m^*\omega_0^2 x_k^2/2$. The V_{TCO} potential is illustrated in Fig. 2(a).

Second, we introduce the trilobal deformation in each MQD through the expression

$$V_{\text{MDQD}}(x, y) = V_{\text{TCO}}(x, y)\{1 + f \sin[3\theta_k' + (-1)^k \pi/2]\}, \quad (5)$$

where θ_k' is the counterclockwise angle around the point $(x_k', 0)$, with x_k' defined as in Eq. (3). The factor f is taken such that the modified interdot barrier $V_b(1 - f)$ equals the minimum barrier between the two MQDs, as determined by the original moiré potential in Eq. (1). The $V_{\text{MDQD}}(x, y)$ employed in all our calculations in this Letter is displayed in Fig. 2(b).

The effective many-body Hamiltonian [40,53–55] associated with the isolated MDQD is given by

$$H_{\text{MB}} = \sum_{i=1}^N \left\{ \frac{\mathbf{p}_i^2}{2m^*} + V_{\text{MDQD}}(\mathbf{r}_i) \right\} + \sum_{i < j}^N \frac{e^2}{\kappa |\mathbf{r}_i - \mathbf{r}_j|}, \quad (6)$$

where m^* is the effective mass of the holes and κ is the dielectric constant. A brief outline of the FCI and sS-UHF methodologies used to solve the corresponding many-body Schrödinger equation is presented in the Supplemental Material [57].

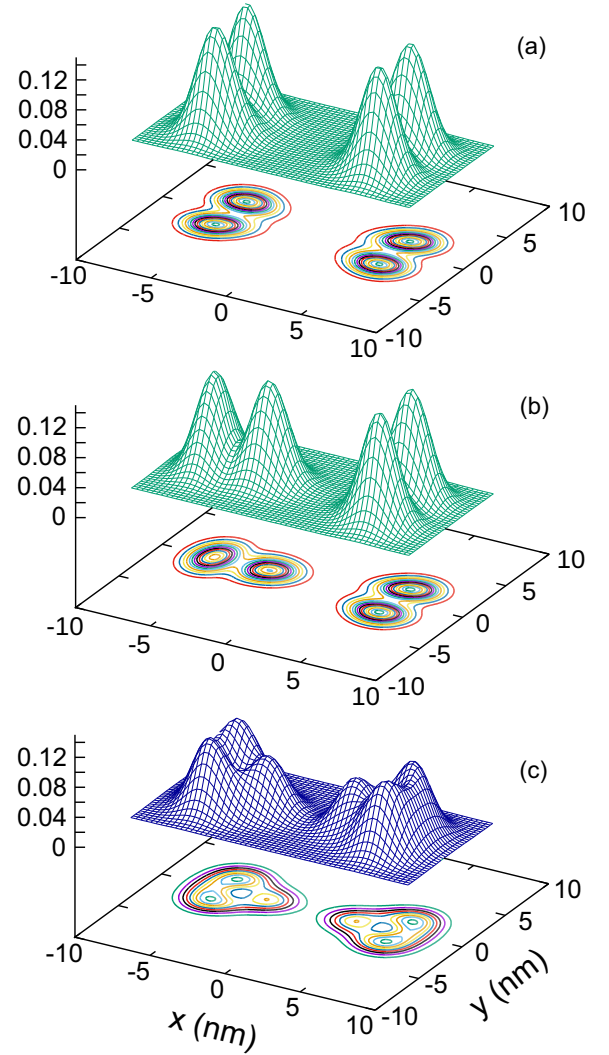


FIG. 4. (a) and (b) Charge densities for $N = 4$ holes associated with the two lowest-energy UHF isomers (with $S_z = 0$) for the MDQD confinement displayed in Fig. 2(b) (which includes the trilobal deformation within each MQD). In both cases, the UHF CDs consist of dumbbell-like pairs of well-localized charge carriers. In panel (a), both the left and right pairs have axes oriented perpendicular to the x axis. In panel (b), the axis of the left dumbbell is parallel to the x axis, whilst the right dumbbell remains perpendicular to the x axis. (c) CD of the x -parity-restored wave function associated with the UHF isomer in panel (b). Note that, unlike the pure UHF CDs in panels (a) and (b), the x -parity-restored CD in panel (c) exhibits a ringlike shape in good agreement with the FCI (exact) CD in Fig. 3(b). See text for a detailed description. Effective mass $m^* = 0.90m_e$ and dielectric constant $\kappa = 5$. CDs are in units of $1/\text{nm}^2$.

FCI results for $N = 4$ holes in the double-dot confinements of Fig. 2. The ground-state FCI charge densities for the four holes confined in the double-MQD of Figs. 2(a) and 2(b) (that is, corresponding to $\nu = 2$ filling of the moiré superlattice) are displayed in Figs. 3(a) and 3(b), respectively; the corresponding FCI total spin is found to be $S = 0$ with the spin projection $S_z = 0$.

Unlike the CDs in Fig. 3(a), which are rather ellipsoidal-like, the CDs in each MQD in Fig. 3(b) do exhibit a trilobal deformation, reflecting the trilobal deformation of the confining potential [Fig. 2(b)]. More importantly, in spite of the Coulombic interaction between the left and right MQDs, which is fully taken into account via our FCI calculation, the $N = 2$ CDs in each MQD of Fig. 3, in both panels (a) and (b), retain the ringlike shape [albeit pearlike distorted in panel (b)] found for an $N = 2$ hole single MQD in our earlier study [40]; see also the inset in Fig. 1(b) shown above.

Naively, these ring-shaped CDs are incompatible with the dumbbell shape of the bonding charge distribution of a “generic” natural molecule (e.g., H_2). However, the case here pertains to a genuinely quantum-mechanical effect: namely, the two-hole antipodal arrangement is hidden (unseen) in the CDs, but its presence is revealed via the conditional probability distributions (CPDs) (which are second-order, density-density correlation functions [58]). Indeed the CPD analysis [40] of such WMs in MQDs (for $2 \leq N \leq 6$) applied to results obtained via FCI (exact) calculations is supplemented and complemented in this Letter through the comparative investigation of exact and mean-field sS-UHF results, with the latter corresponding to approximate solutions of the confined quantum few-body problem. Such UHF vs FCI comparative analysis is part of a constructive hierarchical approach to the complex few-body problem (see Fig. 1 in Ref. [21]).

UHF charge densities for $N = 4$ holes in the double-dot confinement of Fig. 2(b). Charge densities for the two lowest-energy sS-UHF isomers with $S_z = 0$ [59] (for $N = 4$, considered with the same model parameters as in the FCI calculations) in the double MQD confining potential of Fig. 2(b), which includes the $\sin(3\theta'_k)$ trilobal contributions referenced to the center of each QD, are displayed

$$\frac{\langle \Psi(x, y) | \mathcal{O} | \Psi(x, y) \rangle + \langle \Psi(x, y) | \mathcal{O} | \Psi(-x, y) \rangle + \langle \Psi(-x, y) | \mathcal{O} | \Psi(x, y) \rangle + \langle \Psi(-x, y) | \mathcal{O} | \Psi(-x, y) \rangle}{\langle \Psi(x, y) | \Psi(x, y) \rangle + \langle \Psi(x, y) | \Psi(-x, y) \rangle + \langle \Psi(-x, y) | \Psi(x, y) \rangle + \langle \Psi(-x, y) | \Psi(-x, y) \rangle}. \quad (7)$$

The operator associated with the charge density is a one-body operator, $\sum_i^N \delta(\mathbf{r} - \mathbf{r}_i)$, and the charge density is calculated using Eq. (7) and the Löwdin rules [60,61] for calculating matrix elements between Slater determinants with nonorthogonal orbitals. The energy of the symmetry-restored wave function [calculated from Eq. (7) with $\mathcal{O} = H_{MB}$] is lower than the mean-field UHF result, reflecting a gain in correlation energy when going beyond the single-determinant wave function of the UHF method; H_{MB} is the many-body Hamiltonian.

The resulting CD of this x -parity restoration is displayed in Fig. 4(c), and it exhibits an overall shape qualitatively similar to that of the FCI CD in Fig. 3(b) [62]. This result provides a vivid illustration of the limitation of the sS-UHF method to yield a proper description of the Wigner molecules formed in assembled neighboring quantum dots and the imperative need for improvements, such as the one shown here, gained through the application of the beyond-mean-field symmetry-restoration corrective step to the sS-UHF solutions.

FCI and sS-UHF results for $N = 6$ holes in the double-dot confinement of Fig. 2(b). As uncovered in our earlier study

in Figs. 4(a) and 4(b). Unlike the electron charge distribution obtained via the exact-diagonalization (FCI) calculation, the sS-UHF CDs in Figs. 4(a) and 4(b) exhibit prominently a dimer of two well-localized particles within each QD. The difference between these two sS-UHF CDs pertains to the different relative orientations between the axes of the two dimers in the right and left MQDs. Namely, in Fig. 4(a) the left and right dimers are perpendicular to the x axis, while in Fig. 4(b) the left dimer is oriented parallel to the x axis, with the right dimer retaining an orientation perpendicular to the x axis.

It is clear that the sS-UHF CDs do not agree with the FCI CD in Fig. 3(b). This disagreement indicates that, in order to obtain a reliable and satisfactory approximate solution, it is imperative that further corrective steps, beyond the mean-field level, need to be taken. Indeed, a complete theory of such correctional steps is known under the umbrella term of restoration of broken symmetries [21,49,50]. The full set of corrections [21,49,50] which can produce better beyond-UHF approximate solutions and results for both the CDs and the total energies is beyond the scope of this Letter. Nevertheless, an immediately recognizable and available correction is the restoration of the x -parity symmetry of the sS-UHF wave function about the y axis, which is visibly broken in the CD of Fig. 4(b). Such an x -parity restoration can be implemented as described in the following paragraph.

Denoting the UHF Slater determinant as $\Psi(x, y)$, its mirror image about the y axis is given by $\Psi(-x, y)$, and the x -parity-restored wave function is $\propto \Psi(x, y) + p\Psi(-x, y)$, with $p = \pm 1$. Then, because the Slater determinant $\Psi(-x, y)$ is, in general, not orthogonal to $\Psi(x, y)$, the expectation value of an operator \mathcal{O} is given by (here we exhibit the lower-energy case, which was found for the restored wave function with $p = +1$)

[40] on single MQDs, in the case of $\tilde{n} = 3$ holes, the coincidence of the threefold symmetries associated with the C_3 intrinsic geometry of the trimer WM and with the trilobal crystal-field MQD potential [see Fig. 1(b)] results in a *pinned*, empty center, three-hump (0, 3) charge density (see Fig. 2(b) in Ref. [40]). For the double-dot confinement, the calculated exact FCI [see Fig. 5(a)] and approximate sS-UHF [see Fig. 5(b)] charge densities, obtained for $N = 6$ holes ($\tilde{n} = 3$ holes per well, corresponding to $\nu = 3$ filling of the moiré superlattice), are qualitatively very similar. Indeed they maintain close resemblance to the above-noted pinned threefold symmetric configuration in a single MQD. This behavior contrasts with that for $N = 4$ holes in the same MDQD confinement, where the FCI CDs in each well exhibit a sliding WM [see Fig. 3(b)] which differs drastically from the pinned-WM CDs of the sS-UHF approach [see Figs. 4(a) and 4(b)].

Conclusions. The bottom-up research strategy followed in this Letter enables a reliable determination of the influence of interdot Coulomb effects on the formation of quantum WMs in MQDs associated with integer-filling, $\nu > 1$,

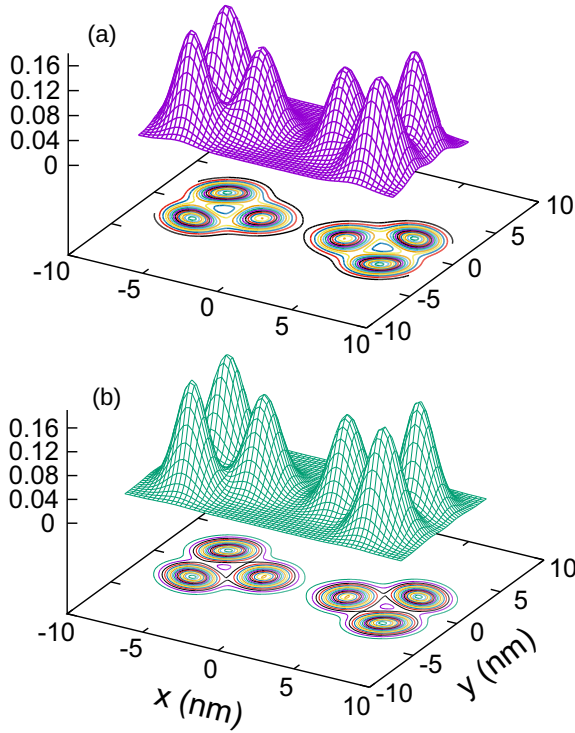


FIG. 5. Charge densities for $N = 6$ fully polarized holes associated with the corresponding lowest-energy state. (a) FCI result (with total spin $S = 3$ and spin projection $S_z = 3$). (b) sS-UHF result (with broken total-spin symmetry and total spin projection $S_z = 3$). The employed MQD double-well confinement is displayed in Fig. 2(b) (which includes the trilobal deformation within each MQD). In both cases, the CDs consist of strongly pinned (0,3) WMs within each potential well. Effective mass $m^* = 0.90m_e$ and dielectric constant $\kappa = 5$. CDs are in units of $1/\text{nm}^2$.

supercrystals in moiré TMD superlattices. Specifically, for the $\nu = 2$ case, we demonstrated explicitly that, in spite of the interdot Coulombic interaction, the exact FCI CDs within each MQD retain the ringlike shape characteristic (for a wide range of relevant parameters [40]) of a fully isolated MQD.

This persisting behavior, which is deeply counterintuitive and quantum mechanical, is associated with the formation of a sliding WM (referred to also as rotating when the confinement exhibits perfect circular symmetry [21]). We also demonstrated that using the mean-field UHF in order to account for the interdot Coulomb interaction is an unreliable approach, with the corresponding CDs portraying orientationally pinned and well-localized dumbbell dimers, in contrast to the exact result. Notably, we illustrated that the gap between exact and UHF results can be bridged by going beyond the mean-field step within a hierarchical strategy that employs the theory of restoration of broken symmetries and its generalizations [21,49]. In contrast to the mean-field results, our corrected sS-UHF methodology, with the parity of the ground-state wave function being restored, yielded (for WMs formed in the coupled MQDs studied here at $\nu = 2$) charge densities that agree with those obtained via exact (FCI) calculations for that system.

We conjecture (to be confirmed both computationally and experimentally) that our conclusions for the $\nu = 2$ superlattice case would extend to other cases, e.g., to all cases with $4 \leq \nu \leq 6$, where our previous study [40] determined that a fully quantum mechanical sliding WM (exhibiting a ringlike CD) is formed in an isolated MQD instead of an azimuthally pinned WM. Finally, we showed that the case of $\nu = 3$ is an exception to the above behavior due to the commensurability between the classical equilibrium configuration of the confined charges and the trilobal C_3 crystal-field-type anisotropy in each MQD potential pocket.

Note added. A recent preprint [63] presents measured STM images for $\nu = 2-4$ integral fillings of hole-doped moiré TMD superlattices that are in remarkable agreement with our predictions here (as well as in our Ref. [40]). Reference [63] presents also sS-UHF calculations for the WM superlattice and comments on their limitations.

Acknowledgments. This work has been supported by a grant from the Air Force Office of Scientific Research (AFOSR) under Grant No. FA9550-21-1-0198. Calculations were carried out at the GATECH Center for Computational Materials Science.

- [1] L. P. Kouwenhoven, C. M. Marcus, P. L. McEuen, S. Tarucha, R. M. Westervelt, and N. S. Wingreen, *Electron transport in quantum dots*, in *Mesoscopic Electron Transport*, edited by L. L. Sohn, L. P. Kouwenhoven, G. Schön (Springer Netherlands, Dordrecht, 1997), p. 105.
- [2] R. Hanson, L. P. Kouwenhoven, J. R. Petta, S. Tarucha, and L. M. K. Vandersypen, *Spins in few-electron quantum dots*, *Rev. Mod. Phys.* **79**, 1217 (2007).
- [3] F.-M. Jing, Z.-Z. Zhang, G.-Q. Qin, G. Luo, G. Cao, H.-O. Li, X.-X. Song, and G.-P. Guo, *Gate-controlled quantum dots based on 2D materials*, *Adv. Quantum Technol.* **5**, 2100162 (2022).
- [4] F. A. Zwanenburg, A. S. Dzurak, A. Morello, M. Y. Simmons, L. C. L. Hollenberg, G. Klimeck, S. Rogge, S. N. Coppersmith, and M. A. Eriksson, *Silicon quantum electronics*, *Rev. Mod. Phys.* **85**, 961 (2013).
- [5] L. M. K. Vandersypen and M. A. Eriksson, *Quantum computing with semiconductor spins*, *Phys. Today* **72**(8), 38 (2019).
- [6] G.-W. Deng, N. Xu, and W.-J. Li, *Gate-defined quantum dots: Fundamentals and applications*, in *Quantum Dot Optoelectronic Devices*, edited by P. Yu and Z. M. Wang (Springer International, Cham, 2020), pp. 107–133.
- [7] G. Burkard, T. D. Ladd, A. Pan, J. M. Nichol, and J. R. Petta, *Semiconductor spin qubits*, *Rev. Mod. Phys.* **95**, 025003 (2023).
- [8] C. Yannouleas and U. Landman, *Spontaneous symmetry breaking in single and molecular quantum dots*, *Phys. Rev. Lett.* **82**, 5325 (1999).
- [9] R. Egger, W. Häusler, C. H. Mak, and H. Grabert, *Crossover from Fermi liquid to Wigner molecule behavior in quantum dots*, *Phys. Rev. Lett.* **82**, 3320 (1999).

- [10] C. Yannouleas and U. Landman, Collective and independent-particle motion in two-electron artificial atoms, *Phys. Rev. Lett.* **85**, 1726 (2000).
- [11] A. V. Filinov, M. Bonitz, and Y. E. Lozovik, Wigner Crystallization in mesoscopic 2D electron systems, *Phys. Rev. Lett.* **86**, 3851 (2001).
- [12] C. Yannouleas and U. Landman, Strongly correlated wavefunctions for artificial atoms and molecules, *J. Phys.: Condens. Matter* **14**, L591 (2002).
- [13] S. A. Mikhailov, Two ground-state modifications of quantum-dot beryllium, *Phys. Rev. B* **66**, 153313 (2002).
- [14] A. Harju, S. Siljamäki, and R. M. Nieminen, Wigner molecules in quantum dots: A quantum Monte Carlo study, *Phys. Rev. B* **65**, 075309 (2002).
- [15] C. Yannouleas and U. Landman, Two-dimensional quantum dots in high magnetic fields: Rotating-electron-molecule versus composite-fermion approach, *Phys. Rev. B* **68**, 035326 (2003).
- [16] M. B. Tavernier, E. Anisimovas, F. M. Peeters, B. Szafran, J. Adamowski, and S. Bednarek, Four-electron quantum dot in a magnetic field, *Phys. Rev. B* **68**, 205305 (2003).
- [17] C. Yannouleas and U. Landman, Structural properties of electrons in quantum dots in high magnetic fields: Crystalline character of cusp states and excitation spectra, *Phys. Rev. B* **70**, 235319 (2004).
- [18] B. Szafran, F. M. Peeters, S. Bednarek, and J. Adamowski, Anisotropic quantum dots: Correspondence between quantum and classical Wigner molecules, parity symmetry, and broken-symmetry states, *Phys. Rev. B* **69**, 125344 (2004).
- [19] I. Romanovsky, C. Yannouleas, L. O. Baksmaty, and U. Landman, Bosonic molecules in rotating traps, *Phys. Rev. Lett.* **97**, 090401 (2006).
- [20] Y. Li, C. Yannouleas, and U. Landman, From a few to many electrons in quantum dots under strong magnetic fields: Properties of rotating electron molecules with multiple rings, *Phys. Rev. B* **73**, 075301 (2006).
- [21] C. Yannouleas and U. Landman, Symmetry breaking and quantum correlations in finite systems: Studies of quantum dots and ultracold Bose gases and related nuclear and chemical methods, *Rep. Prog. Phys.* **70**, 0267 (2007).
- [22] Z. Dai, J.-L. Zhu, N. Yang, and Y. Wang, Spin-dependent rotating Wigner molecules in quantum dots, *Phys. Rev. B* **76**, 085308 (2007).
- [23] Y. Li, C. Yannouleas, and U. Landman, Three-electron anisotropic quantum dots in variable magnetic fields: Exact results for excitation spectra, spin structures, and entanglement, *Phys. Rev. B* **76**, 245310 (2007).
- [24] L. O. Baksmaty, C. Yannouleas, and U. Landman, Rapidly rotating boson molecules with long- or short-range repulsion: An exact diagonalization study, *Phys. Rev. A* **75**, 023620 (2007).
- [25] A. Ghosal, A. D. Güçlü, C. J. Umrigar, D. Ullmo, and H. U. Baranger, Incipient Wigner localization in circular quantum dots, *Phys. Rev. B* **76**, 085341 (2007).
- [26] N. Yang, J.-L. Zhu, and Z. Dai, Rotating Wigner molecules and spin-related behaviors in quantum rings, *J. Phys.: Condens. Matter* **20**, 295202 (2008).
- [27] I. Romanovsky, C. Yannouleas, and U. Landman, Edge states in graphene quantum dots: Fractional quantum Hall effect analogies and differences at zero magnetic field, *Phys. Rev. B* **79**, 075311 (2009).
- [28] B. B. Brandt, C. Yannouleas, and U. Landman, Double-well ultracold-fermions computational microscopy: Wave-function anatomy of attractive-pairing and Wigner-molecule entanglement and natural orbitals, *Nano Lett.* **15**, 7105 (2015).
- [29] C. Yannouleas and U. Landman, Exact closed-form analytic wave functions in two dimensions: Contact-interacting fermionic spinful ultracold atoms in a rapidly rotating trap, *Phys. Rev. Res.* **3**, L032028 (2021).
- [30] H. E. Ercan, S. N. Coppersmith, and M. Friesen, Strong electron-electron interactions in Si/SiGe quantum dots, *Phys. Rev. B* **104**, 235302 (2021).
- [31] J. C. Abadillo-Uriel, B. Martinez, M. Filippone, and Y.-M. Niquet, Two-body Wigner molecularization in asymmetric quantum dot spin qubits, *Phys. Rev. B* **104**, 195305 (2021).
- [32] C. Yannouleas and U. Landman, Wigner molecules and hybrid qubits, *J. Phys.: Condens. Matter* **34**, 21LT01 (2022).
- [33] C. Yannouleas and U. Landman, Molecular formations and spectra due to electron correlations in three-electron hybrid double-well qubits, *Phys. Rev. B* **105**, 205302 (2022).
- [34] C. Ellenberger, T. Ihn, C. Yannouleas, U. Landman, K. Ensslin, D. Driscoll, and A. C. Gossard, Excitation spectrum of two correlated electrons in a lateral quantum dot with negligible Zeeman splitting, *Phys. Rev. Lett.* **96**, 126806 (2006).
- [35] S. Kalliakos, M. Rontani, V. Pellegrini, C. P. García, A. Pinczuk, G. Goldoni, E. Molinari, L. N. Pfeiffer, and K. W. West, A molecular state of correlated electrons in a quantum dot, *Nat. Phys.* **4**, 467 (2008).
- [36] W. Jang, M.-K. Cho, H. Jang, J. Kim, J. Park, G. Kim, B. Kang, H. Jung, V. Umansky, and D. Kim, Single-shot readout of a driven hybrid qubit in a GaAs double quantum dot, *Nano Lett.* **21**, 4999 (2021).
- [37] W. Jang, J. Kim, J. Park, G. Kim, M.-K. Cho, H. Jang, S. Sim, B. Kang, H. Jung, V. Umansky, and D. Kim, Wigner-molecularization-enabled dynamic nuclear polarization, *Nat. Commun.* **14**, 2948 (2023).
- [38] J. Corrigan, J. P. Dodson, H. E. Ercan, J. C. Abadillo-Uriel, B. Thorggrimsson, T. J. Knapp, N. Holman, T. McJunkin, S. F. Neyens, E. R. MacQuarrie, R. H. Foote, L. F. Edge, M. Friesen, S. N. Coppersmith, and M. A. Eriksson, Coherent control and spectroscopy of a semiconductor quantum dot Wigner molecule, *Phys. Rev. Lett.* **127**, 127701 (2021).
- [39] S. Pecker, F. Kuemmeth, A. Secchi, M. Rontani, D. C. Ralph, P. L. McEuen, and S. Ilani, Observation and spectroscopy of a two-electron Wigner molecule in an ultraclean carbon nanotube, *Nat. Phys.* **9**, 576 (2013).
- [40] C. Yannouleas and U. Landman, Quantum Wigner molecules in moiré materials, *Phys. Rev. B* **108**, L121411 (2023).
- [41] C. Yannouleas and U. Landman, Magnetic-field manipulation of chemical bonding in artificial molecules, *Int. J. Quantum Chem.* **90**, 699 (2002).
- [42] C. Yannouleas and U. Landman, Formation and control of electron molecules in artificial atoms: Impurity and magnetic-field effects, *Phys. Rev. B* **61**, 15895 (2000).
- [43] I. Shavitt, The history and evolution of configuration interaction, *Mol. Phys.* **94**, 3 (1998).
- [44] C. Yannouleas and U. Landman, Electron and boson clusters in confined geometries: Symmetry breaking in quantum dots and harmonic traps, *Proc. Natl. Acad. Sci. USA* **103**, 10600 (2006).

- [45] M. Rontani, C. Cavazzoni, D. Bellucci, and G. Goldoni, Full configuration interaction approach to the few-electron problem in artificial atoms, *J. Chem. Phys.* **124**, 124102 (2006).
- [46] C. Yannouleas and U. Landman, Valleytronic full configuration-interaction approach: Application to the excitation spectra of Si double-dot qubits, *Phys. Rev. B* **106**, 195306 (2022).
- [47] A. Szabo and N. S. Ostlund, *Modern Quantum Chemistry* (McGraw-Hill, New York, 1989) For the Slater-Condon rules, see Chap. 4.
- [48] C. Yannouleas and U. Landman, Unified description of floppy and rigid rotating Wigner molecules formed in quantum dots, *Phys. Rev. B* **69**, 113306 (2004).
- [49] J. A. Sheikh, J. Dobaczewski, P. Ring, L. M. Robledo, and C. Yannouleas, Symmetry restoration in mean-field approaches, *J. Phys. G: Nucl. Part. Phys.* **48**, 123001 (2021).
- [50] P. Ring and P. Schuck, *The Nuclear Many-Body Problem* (Springer, Berlin, 1980).
- [51] H. Li, S. Li, E. C. Regan, D. Wang, W. Zhao, S. Kahn, K. Yumigeta, M. Blei, T. Taniguchi, K. Watanabe, S. Tongay, A. Zettl, M. F. Crommie, and F. Wang, Imaging two-dimensional generalized Wigner crystals, *Nature (London)* **597**, 650 (2021).
- [52] K. P. Nuckolls, R. L. Lee, M. Oh, D. Wong, T. Soejima, J. P. Hong, D. Călugăru, J. Herzog-Arbeitman, B. A. Bernevig, K. Watanabe, T. Taniguchi, N. Regnault, M. P. Zaletel, and A. Yazdani, Quantum textures of the many-body wavefunctions in magic-angle graphene, *Nature (London)* **620**, 525 (2023).
- [53] F. Wu, T. Lovorn, E. Tutuc, and A. H. MacDonald, Hubbard model physics in transition metal dichalcogenide moiré bands, *Phys. Rev. Lett.* **121**, 026402 (2018).
- [54] M. Angeli and A. H. MacDonald, Γ -valley transition metal dichalcogenide moiré bands, *Proc. Natl. Acad. Sci. USA* **118**, e2021826118 (2021).
- [55] Y. Zhang, N. F. Q. Yuan, and L. Fu, Moiré quantum chemistry: Charge transfer in transition metal dichalcogenide superlattices, *Phys. Rev. B* **102**, 201115(R) (2020).
- [56] Y. Li, C. Yannouleas, and U. Landman, Artificial quantum-dot helium molecules: Electronic spectra, spin structures, and Heisenberg clusters, *Phys. Rev. B* **80**, 045326 (2009).
- [57] See Supplemental Material at <http://link.aps.org/supplemental/10.1103/PhysRevB.109.L121302> for a brief outline on the FCI, sS-UHF, and symmetry restoration methods.
- [58] Second-order correlations have been used to decipher counterintuitive and spectacular quantum-mechanical behaviors in several fields of physics, e.g., the Hong-Ou-Mandel effect in optics [64,65] or the far-field particle coincidence maps in ultracold atoms [66].
- [59] The two UHF isomers have very close energies, i.e., 526.05 and 526.25 meV, respectively. The FCI ground state has a lower energy of 505.54 meV. We note that the UHF does not preserve the total spin.
- [60] P.-O. Löwdin, Quantum theory of many-particle systems. I. Physical interpretations by means of density matrices, natural spin-orbitals, and convergence problems in the method of configurational interaction, *Phys. Rev.* **97**, 1474 (1955).
- [61] J. Verbeek and J. H. Van Lenthe, On the evaluation of non-orthogonal matrix elements, *J. Mol. Struct.: THEOCHEM* **229**, 115 (1991).
- [62] In spite of this convergence in the shape of CDs, the simple two-Slater-determinant wave function $\Psi(x, y) + \Psi(-x, y)$ is still only an approximation of the FCI one. Indeed, the lowering in total energy is only ≈ 0.012 meV compared to a lowering of ≈ 21 meV that is required to reach the FCI value; see Ref. [59]. This remaining discrepancy can be overcome by restoring the total spin and by accounting for additional quantum fluctuations through mixing constrained Hartree-Fock solutions associated with several different orientations (beyond those parallel or perpendicular to the x axis) of the antipodal dimers; this mixing can be carried out by following the Griffin-Hill-Wheeler generator-coordinate method [21,49,50,67,68], which is even broader in scope than the symmetry-restoration methodology.
- [63] H. Li, Z. Xiang, A. P. Reddy, T. Devakul, R. Sailus, R. Banerjee, T. Taniguchi, K. Watanabe, S. Tongay, A. Zettl, L. Fu, M. F. Crommie, and F. Wang, Wigner molecular crystals from multi-electron moiré artificial atoms, [arXiv:2312.07607](https://arxiv.org/abs/2312.07607).
- [64] C. K. Hong, Z. Y. Ou, and L. Mandel, Measurement of subpicosecond time intervals between two photons by interference, *Phys. Rev. Lett.* **59**, 2044 (1987).
- [65] L. Mandel, Quantum effects in one-photon and two-photon interference, *Rev. Mod. Phys.* **71**, S274 (1999).
- [66] C. Yannouleas, B. B. Brandt, and U. Landman, Interference, spectral momentum correlations, entanglement, and Bell inequality for a trapped interacting ultracold atomic dimer: Analogies with biphoton interferometry, *Phys. Rev. A* **99**, 013616 (2019).
- [67] D. L. Hill and J. A. Wheeler, Nuclear constitution and the interpretation of fission phenomena, *Phys. Rev.* **89**, 1102 (1953).
- [68] J. J. Griffin and J. A. Wheeler, Collective motions in nuclei by the method of generator coordinates, *Phys. Rev.* **108**, 311 (1957).